Research Article | Vol. 25, No. 18 | 4 Sep 2017 | OPTICS EXPRESS 22017
Optics EXPRESS

Abnormal chiral events in a semiconductor laser with coherent injection

CRISTINA RIMOLDI,[1,*] FRANÇOIS GUSTAVE,[2] LORENZO COLUMBO,[3,4] MASSIMO BRAMBILLA,[4,5] STÉPHANE BARLAND,[1] FRANCO PRATI, [6,7] AND GIOVANNA TISSONI[1]

[1] *Université Côte d'Azur, CNRS UMR 7010, Institut de Physique de Nice, 1361 Route des Lucioles, F-06560 Valbonne, France*
[2] *Unversité de Lille, CNRS UMR 8523, Laboratoire de Physique des Lasers, Atomes et Molécules (PhLAM), F-59000 Lille, France*
[3] *Politecnico di Torino, Dipartimento di Elettronica e Telecomunicazioni, Corso Duca degli Abruzzi 24, I-10129 Torino, Italy*
[4] *Istituto di Fotonica e Nanotecnologie del CNR, via Amendola 173, I-70126 Bari, Italy*
[5] *Dipartimento di Fisica Interateneo, Università e Politecnico di Bari, Via Amendola 173, I-70126 Bari, Italy*
[6] *Diparimento di Scienza e Alta Tecnologia, Università dell'Insubria, Via Valleggio 11, I-22100 Como, Italy*
[7] *CNISM, Research Unit of Como, Via Valleggio 11, I-22100 Como, Italy*
[*] *cristina.rimoldi@inphyni.cnrs.fr*

Abstract: We study experimentally and theoretically the dynamics of a spatially extended (along the propagation direction) oscillatory medium with coherent forcing. We observe abnormally high events, responsible for a different statistics of intensity and pulse height, in a regime where solitons and roll patterns are unstable. We focus on the formation of these high-peak events and their connection to the phase dynamics. Each abnormal event can be associated with a change in the slope of the phase time trace. Furthermore, the coexistence of $\pm 2\pi$ phase rotations inside the cavity can be associated to the observation of abnormal events, similarly to recent predictions in bidimensional vortex turbulence.

OCIS codes: (140.5960) Semiconductor lasers; (190.5530) Pulse propagation and temporal solitons; (190.3100) Instabilities and chaos; (190.5970) Semiconductor nonlinear optics including MQW.

References and links

1. D. R. Solli, C. Ropers, P. Koonath, and B. Jalali, "Optical rogue waves," Nature **450**, 1054–1057 (2007).
2. C. Kharif, E. Pelinovsky, and A. Slunyaev, *Rogue Waves in the Ocean (Advances in Geophysical and Environmental Mechanics and Mathematics)* (Springer, 2009).
3. S. Birkholz, C. Brée, I. Veselić, A. Demircan, and G. Steinmeyer, "Ocean rogue waves and their phase space dynamics in the limit of a linear interference model," Sci. Rep. **6**, 35207 (2016).
4. R. Höhmann, U. Kuhl, H.-J. Stöckmann, L. Kaplan, and E. Heller, "Freak waves in the linear regime: A microwave study," Phys. Rev. Lett. **104**, 093901 (2010).
5. N. Akhmediev, A. Ankiewicz, and J. M. Soto-Crespo, "Rogue waves and rational solutions of the nonlinear schrödinger equation," Phys. Rev. E **80**, 026601 (2009).
6. D. J. Kedziora, A. Ankiewicz, and N. Akhmediev, "Classifying the hierarchy of nonlinear-schrödinger-equation rogue-wave solutions," Phys. Rev. E **88**, 013207 (2013).
7. B. Kibler, J. Fatome, C. Finot, G. Millot, F. Dias, G. Genty, N. Akhmediev, and J. M. Dudley, "The peregrine soliton in nonlinear fibre optics," Nat. Phys. **6**, 790–795 (2010).
8. S. Randoux, P. Suret, and G. El, "Identification of rogue waves from scattering transform analysis of periodized waveforms," arXiv preprint https://arXiv:1512.04707 (2015).
9. M. Närhi, B. Wetzel, C. Billet, S. Toenger, T. Sylvestre, J.-M. Merolla, R. Morandotti, F. Dias, G. Genty, and J. M. Dudley, "Real-time measurements of spontaneous breathers and rogue wave events in optical fibre modulation instability," Nat. Commun. **7**, 13675 (2016).
10. A. Mussot, A. Kudlinski, M. Kolobov, E. Louvergneaux, M. Douay, and M. Taki, "Observation of extreme temporal events in cw-pumped supercontinuum," Opt. Express **17**, 17010–17015 (2009).
11. J. M. Dudley, G. Genty, F. Dias, B. Kibler, and N. Akhmediev, "Modulation instability, akhmediev breathers and continuous wave supercontinuum generation," Opt. Express **17**, 21497–21508 (2009).

#296836 https://doi.org/10.1364/OE.25.022017
Journal © 2017 Received 31 May 2017; revised 15 Aug 2017; accepted 15 Aug 2017; published 31 Aug 2017

Optics EXPRESS

12. K. Hammani, B. Kibler, C. Finot, and A. Picozzi, "Emergence of rogue waves from optical turbulence," Phys. Lett. A **374**, 3585–3589 (2010).
13. P. Walczak, S. Randoux, and P. Suret, "Optical rogue waves in integrable turbulence," Phys. Rev. Lett. **114**, 143903 (2015).
14. P. Suret, R. El Koussaifi, A. Tikan, C. Evain, S. Randoux, C. Szwaj, and S. Bielawski, "Single-shot observation of optical rogue waves in integrable turbulence using time microscopy," Nat. Commun. **7**, 13136 (2016).
15. M. G. Kovalsky, A. A. Hnilo, and J. R. Tredicce, "Extreme events in the ti: sapphire laser," Opt. Lett. **36**, 4449–4451 (2011).
16. C. Lecaplain, P. Grelu, J. M. Soto-Crespo, and N. Akhmediev, "Dissipative rogue waves generated by chaotic pulse bunching in a mode-locked laser," Phys. Rev. Lett. **108**, 233901 (2012).
17. F. Selmi, S. Coulibaly, Z. Loghmari, I. Sagnes, G. Beaudoin, M. G. Clerc, and S. Barbay, "Spatiotemporal chaos induces extreme events in an extended microcavity laser," Phys. Rev. Lett. **116**, 013901 (2016).
18. S. Coulibaly, M. Clerc, F. Selmi, and S. Barbay, "Extreme events following bifurcation to spatiotemporal chaos in a spatially extended microcavity laser," Phys. Rev. A **95**, 023816 (2017).
19. C. Rimoldi, S. Barland, F. Prati, and G. Tissoni, "Spatiotemporal extreme events in a laser with a saturable absorber," Phys. Rev. A **95**, 023841 (2017).
20. C. Bonatto, M. Feyereisen, S. Barland, M. Giudici, C. Masoller, J. R. R. Leite, and J. R. Tredicce, "Deterministic optical rogue waves," Phys. Rev. Lett. **107**, 053901 (2011).
21. J. Zamora-Munt, B. Garbin, S. Barland, M. Giudici, J. R. R. Leite, C. Masoller, and J. R. Tredicce, "Rogue waves in optically injected lasers: Origin, predictability, and suppression," Phys. Rev. A **87**, 035802 (2013).
22. J. Ahuja, D. B. Nalawade, J. Zamora-Munt, R. Vilaseca, and C. Masoller, "Rogue waves in injected semiconductor lasers with current modulation: role of the modulation phase," Opt. Express **22**, 28377–28382 (2014).
23. G.-L. Oppo, A. M. Yao, and D. Cuozzo, "Self-organization, pattern formation, cavity solitons, and rogue waves in singly resonant optical parametric oscillators," Phys. Rev. A **88**, 043813 (2013).
24. C. J. Gibson, A. M. Yao, and G.-L. Oppo, "Optical rogue waves in vortex turbulence," Phys. Rev. Lett. **116**, 043903 (2016).
25. F. Gustave, L. Columbo, G. Tissoni, M. Brambilla, F. Prati, B. Kelleher, B. Tykalewicz, and S. Barland, "Dissipative phase solitons in semiconductor lasers," Phys. Rev. Lett. **115**, 043902 (2015).
26. F. Gustave, C. Rimoldi, P. Walczak, L. Columbo, M. Brambilla, F. Prati, G. Tissoni, and S. Barland, "Formation of phase soliton complexes in an optically injected semiconductor laser," Eur. Phys. J. D, **71**(6), 154 (2017).
27. F. Gustave, L. Columbo, G. Tissoni, M. Brambilla, F. Prati, and S. Barland, "Phase solitons and domain dynamics in an optically injected semiconductor laser," Phys. Rev. A **93**, 063824 (2016).
28. A. Coillet, J. Dudley, G. Genty, L. Larger, and Y. K. Chembo, "Optical rogue waves in whispering-gallery-mode resonators," Phys. Rev. A **89**, 013835 (2014).
29. H. Chaté, A. Pikovsky, and O. Rudzick, "Forcing oscillatory media: phase kinks vs. synchronization," Phys. D Nonlinear Phenom. **131**, 17–30 (1999).
30. S. Longhi, "Nonlinear travelling pulses in laser injection locking," Quantum and Semiclassical Optics: J. Euro. Opt. Soc. Part B (1995-1998) **10**, 617–635 (1998).
31. P. Walczak, C. Rimoldi, F. Gustave, L. Columbo, M. Brambilla, F. Prati, G. Tissoni, and S. Barland, "Extreme events induced by collisions in a forced semiconductor laser," Submitted to Opt. Lett. (May 2017). https://arxiv.org/abs/1705.02153 .
32. F. Gustave, "Phase dynamics and dissipative solitons in semiconductor lasers," Ph.D. thesis, Université de Nice Sophia Antipolis (2016).
33. S. Barland, O. Piro, M. Giudici, J. R. Tredicce, and S. Balle, "Experimental evidence of van der pol–fitzhugh–nagumo dynamics in semiconductor optical amplifiers," Phys. Rev. E **68**, 036209 (2003).
34. L. Spinelli, G. Tissoni, L. A. Lugiato, and M. Brambilla, "Thermal effects and transverse structures in semiconductor microcavities with population inversion," Phys. Rev. A **66**, 023817 (2002).
35. G. Tissoni, L. Spinelli, L. A. Lugiato, M. Brambilla, I. M. Perrini, and T. Maggipinto, "Spatio-temporal dynamics in semiconductor microresonators with thermal effects," Opt. Express **10**, 1009–1017 (2002).
36. V. Brasch, M. Geiselmann, M. H. Pfeiffer, and T. J. Kippenberg, "Bringing short-lived dissipative kerr soliton states in microresonators into a steady state," Opt. Express **24**, 29312–29320 (2016).
37. P. Coullet, L. Gil, and J. Lega, "Defect-mediated turbulence," Phys. Rev. Lett. **62**, 1619–1622 (1989).
38. S. V. Fedorov, A. G. Vladimirov, G. V. Khodova, and N. N. Rosanov, "Effect of frequency detunings and finite relaxation rates on laser localized structures," Phys. Rev. E **61**, 5814–5824 (2000).
39. L. Spinelli, G. Tissoni, M. Brambilla, F. Prati, and L. A. Lugiato, "Spatial solitons in semiconductor microcavities," Phys. Rev. A **58**, 2542–2559 (1998).

1. Introduction

With the seminal work on optical rogue waves [1], optical devices have become a system of choice for the analysis of large amplitude and unexpected events occurring in complex wave propagation settings. One possible and fruitful approach puts emphasis on the properties of

Optics EXPRESS

individual events such as their shape, their reduced spatial extension and temporal duration or the presence of "sister waves" surrounding the main event, in analogy with the so-called "Draupner wave" [2]. From this point of view one can cite the study of the superposition of linear waves [3,4] and the theoretical and experimental analysis of different kinds of solitons and breathers (recent works include [5–9]).

In a complementary way, other studies focus more on the statistical properties of the field, often aiming at determining the general dynamical mechanisms which favor the emergence of unexpectedly large events or at predicting their occurrence with some anticipation. In conservative systems for instance the regimes of modulation instability [1, 10, 11], optical turbulence [12] and integrable turbulence [13, 14] have been shown to lead to heavy tailed distributions. In dissipative systems, rogue waves have been observed in lasers with saturable absorber along the propagation direction [15, 16] and also in bidimensional systems, in the plane transverse to propagation [17–19]. In the former case they have been related to chaotic pulsing and in the latter to spatio-temporal chaos [18] and dissipative solitons [19]. The case of oscillatory media (optical parametric oscillators or lasers) with nearly resonant forcing has also been examined in different numbers of spatial dimensions. In purely temporal systems heavy tailed statistics have been attributed to low dimensional deterministic chaos near a critical transition [20, 21]. In this case noise or deterministic parameter modulation have been shown to heavily impact the presence of rogue events [22]. In two transverse dimensions, the occurrence of rogue events has been associated to vortex turbulence and in particular to the collision of spiral waves [23, 24]. Here we address the emergence of abnormally high events in a complementary case, *i.e.* the one dimensional case along propagation. We prepare a highly multimode ring semiconductor laser and apply to it a coherent optical injection beam. A wealth of dynamical regimes has been observed in this configuration, including solitary waves [25], complexes of solitary waves [26], plane waves, modulational instabilities and front propagation [27]. In contrast with passive nonlinear resonators (see *e.g.* [28] in the context of extreme events), the solitary waves observed experimentally to date are not locked to the forcing. Due to the oscillatory nature of the medium, they consist of 2π (or $n * 2\pi$ in the case of complexes) rotations of the optical phase with respect to the optical phase of the forcing beam [29]. In the propagative geometry with non-instantaneous nonlinearity, only one sign of phase rotation is found to be stable [27, 30]. Here we measure experimentally the statistical distribution of the emitted intensity and relate it to the measured phase dynamics. We analyze our experimental results thanks to numerical simulations of a set of partial differential equations for the electric field envelope and the carrier density. We consider a parametric regime where the locked solution is unstable, and a non stationary irregular roll pattern develops instead. This regime is the same observed experimentally, and it differs from recent observations reported in a similar system [31], where extreme events are observed in a regime where the locked solution and phase solitons are stable, and very high intensity peaks develop through collisions of localized structures of different nature and velocity.

In section 2 we show the experimental results, their statistical and dynamical analysis, and we focus on the role of the phase in the formation of abnormal events, and on their predictability. In section 3 we present the theoretical model describing our system, and show numerical results about intensity dynamics and its statistics, in excellent agreement with the experiment. We then focus on the phase dynamics and individuate the role of $\pm 2\pi$ phase rotations in the formation of abnormal events. Finally, in section 4 we draw some conclusions and perspectives.

2. Experimental results

2.1. The setup

The experimental setup depicted in Fig. 1 is based on a highly multimode semiconductor ring laser under coherent external forcing and has been described extensively in [25, 27, 32]. The ring laser is made of a semiconductor optical amplifier (SOA) acting as gain medium centered around

Optics EXPRESS

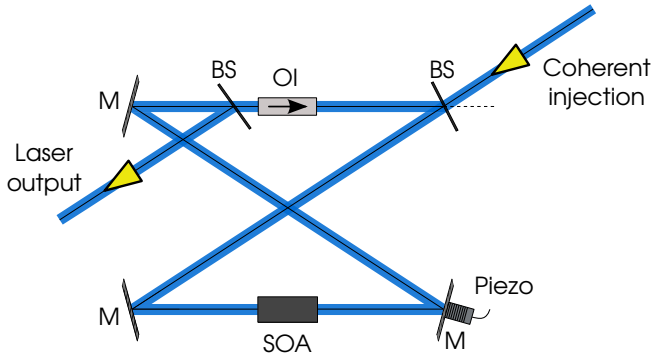

Fig. 1. Scheme of the experimental setup. SOA semiconductor optical amplifier, M mirrors, BS beam splitters, OI optical isolator, Piezo piezoelectric actuator. See text for details.

980 nm and enclosed in a 1 m long ring cavity. The anti-reflection coating on the SOA facets prevents from self-lasing of the semiconductor element. An optical isolator has been placed inside the ring cavity to ensure unidirectional operation and the spatial filtering imposed by its physical aperture forces the ring laser to emit on a single transverse mode. Two beam splitters are inserted in the ring cavity, the first one has 90% reflectivity and allows the injection of the external coherent field while the second one has 10% reflectivity to provide the ring laser output. The ring laser is operated at a bias current of 1.1 times the threshold current value (around 1.6 to 1.8 A depending on precise alignment conditions). The coherent injected field comes from a homemade tunable single mode laser allowing a coarse control of the detuning between the injection and the ring laser. The fine control of the detuning is obtained by adjusting the cavity length by use of a piezo electric actuator placed on one of the mirrors mount. However, due to optothermal nonlinearity [27, 33–35], the value of the detuning can not be kept constant for sufficiently long time to allow meaningful measurements (a situation which may be addressed in the future by temporal engineering of the detuning parameter as in [36]).

We analyze the output of the ring laser by means of fast photodiodes connected to a 12.5 GHz bandwidth real-time oscilloscope with 100 GS/s sampling rate. Instead of measuring directly the optical power, we use an heterodyne setup based on a 3×3 fiber coupler to access both the power and the relative phase between the forcing and the ring laser (see [25, 27] for more details).

The longitudinal extension of the ring laser acts as an effective propagation dimension in space, with mode-defining boundaries, along which the optical field can present many different multimodal behaviors depending on the two main control parameters of the system: the injection strength (optical power) and the frequency detuning between the injection and the closest resonance of the ring cavity. For strong enough injection power (about 5mW measured before the incoupling beam splitter, depending on mode matching conditions), the laser can be fully synchronized (in phase and frequency) to the forcing. In this case, we observe a stable uniform state characterized by a flat intensity profile and constant phase difference between the laser and the forcing. When reducing the forcing strength, the formation of dissipative phase solitons (PSs) has been observed and described as localised 2π phase rotations corresponding to local unlocking of the laser to its forcing. Roll patterns have also been observed and described as the result of modulational instability [27]. These periodic patterns correspond to a phase bounded regime for which the phase circles on a closed loop in a bounded region of the complex plane [32].

Optics EXPRESS

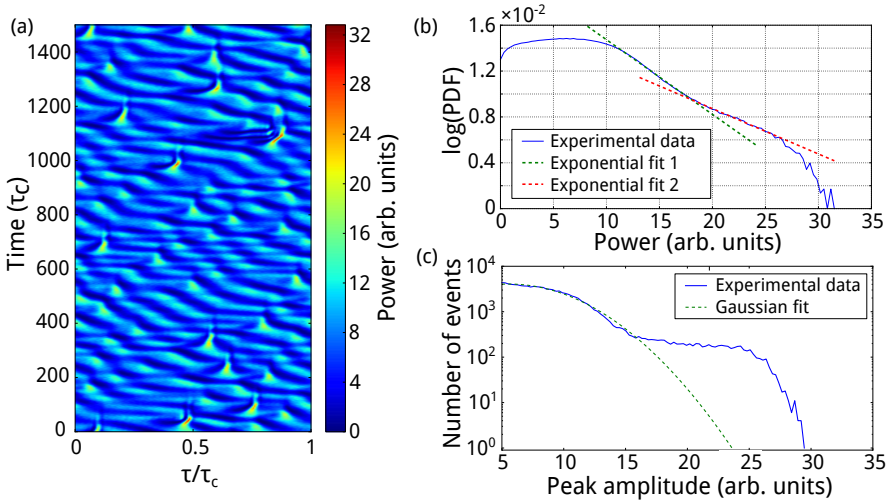

Fig. 2. Dynamical and statistical properties of abnormal events. (a) Spatio-temporal diagram of the optical power along 1500 roundtrips, (b) logarithm of the probability density function of the total power and (c) distribution of the peak amplitudes. Both (b) and (c) are computed on long time traces of length $\simeq 27\,000 \times \tau_c$ (5×10^6 points)

2.2. *Statistical analysis*

We present here the observation of a dynamical regime in which an unstable roll pattern hosts high intensity peaks appearing randomly in space and time. Figure 2(a) shows a spatio-temporal diagram of this regime, where the horizontal axis refers to the longitudinal spatial dimension of the laser and the vertical axis represents time in units of the cavity roundtrip time $\tau_c \simeq 3.6$ ns. In this figure, we can clearly identify the unstable roll pattern in background and high intensity pulses nucleated on top of it. In order to get the statistical signatures of this regime, we computed the probability density function (PDF) of the total optical power and the distribution of the peak amplitudes, respectively represented in Figs. 2(b)-2(c). In the PDF of the power, we first distinguish a plateau (up to 10), followed by an exponential decay (up to 17) and a second exponential decay with smaller slope corresponding to a clearly different statistics. The presence of this statistical deviation at high amplitudes implies that high intensity pulses occur more often than if the distribution followed the first exponential decay. Although the shape of this distribution is non trivial, we understand easily that different mechanisms are necessary to produce these three different behaviors.

The statistics of the peak heights is shown in Fig. 2(c). The heights are measured by computing the difference between each maximum and the previous minimum of the full time trace. Note that we disregard events of height below 5, inasmuch we have no way to discriminate the actual field dynamics from the detection noise. Doing so, we do not need to apply any spectral filtering on the data that would modify the distribution. The shape of the distribution is well fitted by a Gaussian up to 16 and presents a huge deviation beyond this point. The Gaussian part of the distribution (at low values) is related to the oscillating background whereas the deviation appearing at high values corresponds to the presence of abnormal events. Since the threshold we use as definition is clearly identified as an inflexion point separating the tail from the rest of the distribution, those events belonging to this tail may be expected to actually differ from others in nature and not only in amplitude.

Optics EXPRESS

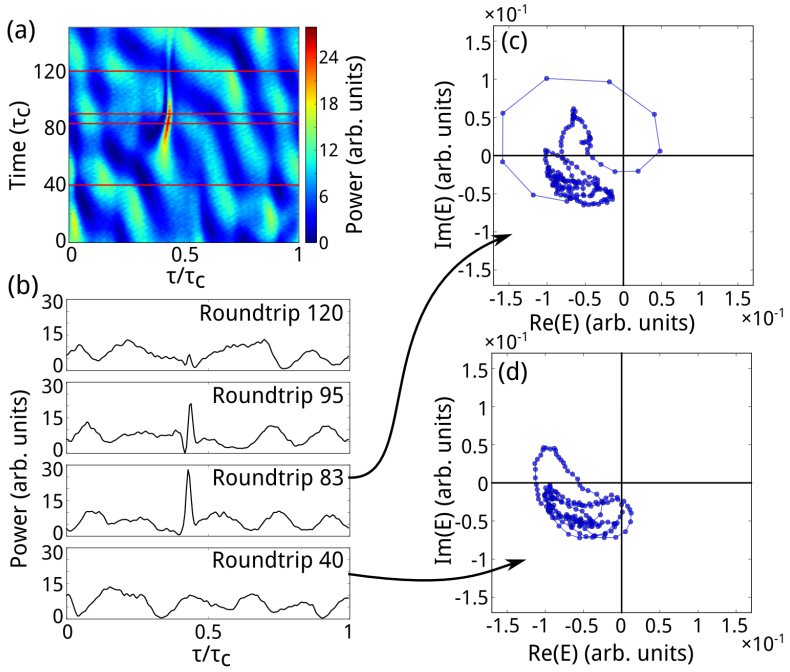

Fig. 3. Power and phase dynamics around the formation of an abnormal event. (a) spatio-temporal diagram focused on one event, taken around roundtrip 1000 of Fig. 2(a), (b) Power profiles corresponding to roundtrip 40, 83, 95 and 120 and depicted by red horizontal lines in (a), (d) phase trajectory in the Argand plane before the abnormal event (roundtrip 40) and (c) at the maximum peak power of the event (roundtrip 83). (See also Visualization 1 in supplementary materials).

2.3. *Dynamical analysis*

To understand the formation of these abnormal events, we focus on one particular event, statistically representative of the relevant regime, and provide a detailed analysis by looking at both phase and intensity dynamics. Figure 3(a) shows a zoom of the spatio-temporal diagram presented in Fig. 2(a) on 150 roundtrips around an abnormal event. The horizontal red lines represent the positions at which intensity profiles shown in Fig. 3(b) have been taken. The first line (roundtrip 40) shows the state of the system before the abnormal event occurs and the associated phase trajectory is presented in Fig. 3(d). At this stage of evolution, the phase remains in a bounded region of the complex plane (Argand plane). Note that the phase measurement we realize gives us the phase difference between the injection and laser relative to an arbitrary reference phase. This means that the position of the bounded state in the complex plane is not relevant, and the whole trajectory could be arbitrarily rotated around the origin without changing its shape. At roundtrip 83, the abnormal event has reached its maximum intensity. By comparing the height of this event with the statistics shown in Fig. 2(c), we can easily understand that this object participates to the strong statistical deviation described before.

As we can see in Fig. 3(c), the high intensity peak is accompanied by a striking topological change of the phase space picture, namely we observe that the trajectory circles around the origin. The system seems to be pushed away from the bounded state and explore a wider region of the complex plane. The process occurs with a phase bounded rotation growing in amplitude and changing shape until it actually includes the origin. Thus, the abnormal event acquires a counterclockwise ($+2\pi$) phase rotation. This phase trajectory resembles the one of PSs, that

Optics EXPRESS

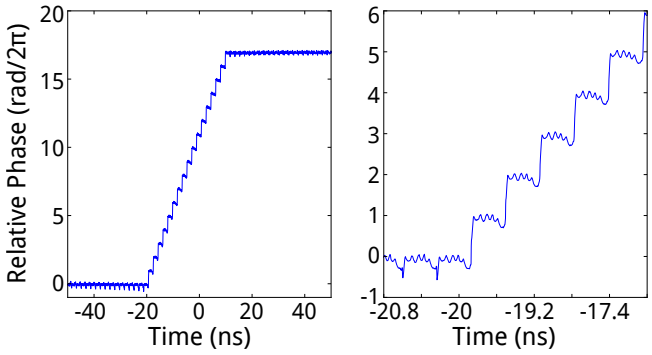

Fig. 4. Evolution of the phase when approaching the abnormal event. Left : 100 ns long time trace of the phase centered on the maximum of an abnormal event showing the acquisition of positive phase rotations. Right : zoom of the same time trace at the beginning of the change of slope. The initial phase is arbitrarily set to zero.

are actually not stable for this set of parameters. PSs have been found to carry only positive chiral charges (counterclockwise phase rotations) due to the strong symmetry breaking caused by the propagative nature of the system [25]. The phase trajectories of the observed abnormal events give a strong argument to describe them as unstable PSs nucleated from the unstable roll pattern. In section 3, a theoretical analysis and numerical simulations are presented to clarify the structure of the phase space and explain this connection in a deeper way.

In Fig. 4, we show the evolution of the unfolded phase around the formation of an abnormal event. The time trace is centered on the abnormal event maximum intensity ($t = 0$). In this representation, it is clear that the phase stays bounded up to 20 ns before the maximum of the abnormal event. We can clearly identify the phase rotations as a change of slope, that starts before the moment where the abnormal event reaches its maximum. At each roundtrip, the system acquires 2π rotations corresponding in this representation to steps of 2π. The phase and amplitude dynamics leading to the emergence of these abnormal events are reminiscent of the defect mediated turbulence discussed theoretically in the context of forced oscillatory media [24, 37].

3. Theory

3.1. Model

The model used to describe our system is given by the following set of rate equations [25, 27], which is derived from the effective Maxwell-Bloch equations, when the polarization of the material is adiabatically eliminated:

$$\frac{\partial E}{\partial z} + \frac{\partial E}{\partial t} - d\frac{\partial^2 E}{\partial z^2} = T\left[-(1+i\theta)E + y + (1-i\alpha)ED\right] \quad (1)$$

$$\frac{\partial D}{\partial t} = b\left[\mu - D\left(1+|E|^2\right)\right] \quad (2)$$

where E and D are, respectively, the slowly varying envelope of the electric field and the excess of carrier density with respect to transparency. T represents the cavity losses, y is the amplitude of the injected field, arbitrarily taken real and positive, and θ represents the frequency mismatch of the injected field with respect to the closest empty cavity resonance. α is the linewidth enhancement factor, μ is the pump parameter and b represents the ratio of the roundtrip time to the carrier lifetime. As typical parameter values used here, and constant throughout the paper,

Optics EXPRESS

we took: $\alpha = 3$, $b = 10$, $T = 0.3$. Variables are scaled in such a way that the boundary condition becomes periodic and isochronous. An extensive study and derivation of this model can be found in [25, 27].

At difference from [25, 27], a diffusion term appears on the left hand side of Eq. (1). While we introduce it phenomenologically, its derivation proceeds from a nonstandard elimination of the polarization which takes into account the finite gain linewidth [38]. Physically this term is weighed by a coefficient which is proportional to the squared ratio of the cavity free spectral range to the gain linewidth.

Equations (1)-(2) admit the stationary homogeneous solution $E = E_s = \rho_s \exp(i\phi_s)$, $D = D_s$ with

$$y^2 = \rho_s^2 \left[(1 - D_s)^2 + (\theta + \alpha D_s)^2\right] \tag{3}$$

$$\phi_s = \arctan\left(\frac{\theta + \alpha D_s}{D_s - 1}\right) \tag{4}$$

$$D_s = \frac{\mu}{1 + \rho_s^2} \tag{5}$$

where we observe that $\mu = 1$ corresponds to the threshold value for the pump parameter in the free running laser. In Fig. 5(a) we plotted the stationary intensity $I = \rho_s^2$ of the electric field as a function of the injection amplitude y according with Eq. (3). The values of the pump parameter,

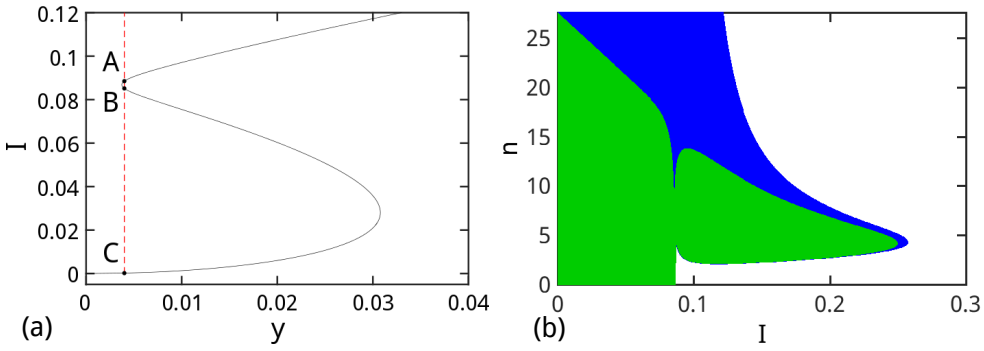

Fig. 5. (a) Stationary homogenous solution of Eqs. (1)-(2) as indicated in Eq. (3) for the parameters $\mu = 1.1$, and $\theta = -3.04$ (see the text for the other parameters). Points A, B and C represent the three injection locked solutions corresponding to the value of injection used in the simulations $y = 0.004$, highlighted by the red dashed vertical line. (b) Instability domains in the (I, n) plane for the model described in Eqs. (1)-(2) (in green) and for the pure rate equation model with $d = 0$ (in blue).

detuning and injection amplitude have been chosen to keep the system very close to the left turning point of the stationary homogeneous solution: $\mu = 1.1$, $\theta = -3.04$ and $y = 0.004$. Points A, B and C indicate the three fixed points for the chosen value of injection amplitude (vertical red dashed line): in particular A is a node, B is a saddle and C is a focus [25, 27].

In Fig. 5(b) the stability scenery of the homogeneous stationary solution is plotted in the (I, n) plane, where n is the order of the longitudinal sidemode. The green domain indicates the unstable region as derived from the linear stability analysis of the locked solutions (3)-(5) in presence of diffusion ($d \neq 0$), with the reported parameters, while the blue domain corresponds to the choice $d = 0$, which amounts to the pure rate equation model without spectral filtering [25, 27]. It is clear that the diffusive term sets a limit to the number of unstable longitudinal modes. Actually, for a cavity length of 1 m and assuming a gain linewidth of 10 THz, the number of modes under the gain line should be much larger, *i.e.* the diffusion coefficient d should be smaller by some

Optics EXPRESS

order of magnitude. We chose here $d = 10^{-6}$ in order to filter the higher order modes, which are not relevant for the dynamics. In that way we could limit the number of grid points in the numerical simulations to a reasonable value (1024 points). Fig. 5(b) shows that our choice is justified because the large value of d affects only slightly the instability domain for the larger intensity values, i.e. in the upper branch of the stationary solution.

From Fig. 5 we can observe that all the three fixed points A, B and C are unstable for the parametric set considered. For a more detailed description on the stability analysis of this system see [27].

3.2. Numerical simulations

The numerical simulations of Eqs. (1)-(2) confirm that for this system a variety of different regimes is possible. From Eqs. (3)-(5) it is clear that for the free running laser ($y = 0$) the stationary equation gets reduced to $D_s = 1$ (which implies $|E_s|^2 = \mu - 1$) and $\theta + \alpha = 0$. Thus $\theta+\alpha$ is the frequency mismatch between the driving field and the free running laser [39]. When the injected field is red detuned ($\theta + \alpha > 0$), the whole upper branch of the homogeneous stationary solution is stable and the system can sustain phase solitons (PSs), provided the amplitude of the injected field is such that the fixed points A and B, described above, are sufficiently close, i.e. the system is close to the left turning point of the homogeneous stationary solution [25–27, 32]. Phase solitons are homoclinic trajectories connecting the locked homogeneous state A with itself. We want to stress that unlike purely spatial systems [24], in a non-instantaneous propagative (temporal) system as in this case, the chiral charge of the phase soliton can only be positive (*i.e.* corresponding to counterclockwise phase rotations) [27, 30].

In the opposite situation ($\theta + \alpha < 0$), a multimode instability affects a part of the upper branch close to the left turning point, as shown in Fig. 5(b). The PSs are no longer stable and instead a roll pattern arises due to the beating of the fundamental mode with high order sidemodes [32]. Eventually even the rolls become unstable when the injection amplitude is brought too close to the left turning point, and more complex spatio-temporal dynamics can be observed, as in the experiments.

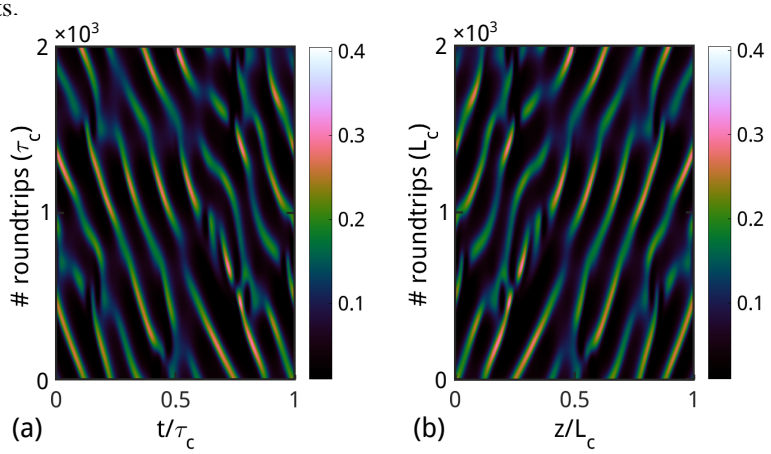

Fig. 6. Spatiotemporal diagrams in (a) the experimental reference frame at fixed z and (b) in the numerical reference frame, where the diagram is built through the stacking of the full cavity spatial profiles acquired each roundtrip.

In this paper we will focus on the latter dynamical regime, illustrated in Figs. 6 and 7.

In Fig. 6 we plotted the spatio-temporal diagrams relative to 2000 cavity roundtrips in two different reference frames. The first reference frame (represented in Fig. 6(a)) corresponds to the experimental one, where data are taken at $z = L$, as one would have from a detector placed

Optics EXPRESS

right at the output of the cavity (save for the mirror transmission). The second reference frame (represented in Fig. 6(b)) can be used only numerically: at each roundtrip, the entire spatial intensity profile inside the cavity is recorded, and then all the recorded profiles (much like snapshots taken every roundtrip time) are stacked onto one other, in such a way to obtain the spatio-temporal diagram illustrated. It is noticeable that the two spatio-temporal diagrams are mirror images one of the other, as it must be in the case of propagating structures.

From now on, we will only consider the experimental reference frame in order to make easier the comparison with the experimental data.

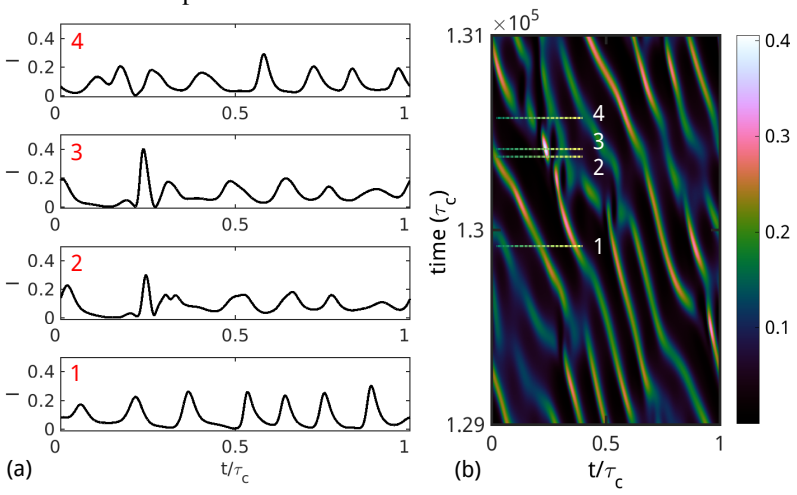

Fig. 7. Zoom (b) of the spatio-temporal diagram centered on an event of high intensity (3) and intensity time traces (a) at fixed roundtrip corresponding to the horizontal cuts highlighted on the diagram. (For the phase dynamics see Visualization 2 in supplementary materials).

In Fig. 7 we show a zoom of the spatio-temporal diagram centered on an event of high intensity occurring at the point highlighted by line 3. This picture shows an interval of 2000 roundtrips in a simulation of 3×10^5 roundtrips where the first 9×10^4 roundtrips were excluded from the following statistical analysis to discharge transient effects.

The four temporal profiles illustrated in Fig. 7(a) correspond to the horizontal cuts highlighted in Fig. 7(b). In particular the temporal profile from section 1 occurs 500 roundtrips before the event and corresponds to a mostly bounded regime, where we can appreciate the remnants of the roll pattern which would be stable for a larger injection amplitude. Section 3 is taken at the maximum of the high intensity event, while sections 2 and 4 are taken, respectively, 40 roundtrips before the event and 160 roundtrips after it.

As for the statistical analysis, we plot (in black) in Fig. 8 the PDF of the temporal peak heights (maximum minus precedent minimum) (a) and of the overall intensity values (b). For comparison we have also included in these plots the corresponding PDFs for a second set of data (plotted in dark yellow), simulated for the same parameters as the data in black but a different value of detuning $\theta = -3.049$: this simulation corresponds to an unstable roll regime, which remains clearly bounded and does not exhibit big excursions in intensity.

As in the corresponding experimental Fig. 2, we observe that the PDF of the heights (a) presents an initial slope that follows a Gaussian distribution (green dashed line), to be associated with the bounded state, while the events in the tail of the distribution appear more frequently than expected by a Gaussian statistics. Furthermore, in the statistics of the total intensity we notice two different negative exponential slopes in the tail of the distribution, as observed in the experiments: the first slope (green dashed line fit), may be be associated with the roll pattern, the

Optics EXPRESS

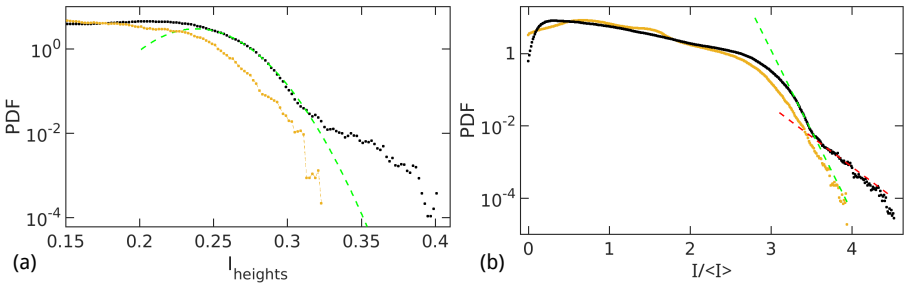

Fig. 8. PDF of the temporal peak heights (in black), computed over 2.1×10^6 roundtrips (a), the green dashed line corresponds to a Gaussian fit of the initial slope. PDF (in black) of all the values explored by the intensity (b), computed over 2.1×10^5 roundtrips. The green and red dashed lines correspond to two negative exponential fits highlighting the change of the slopes in the tail of the distribution. The data in dark yellow shows the corresponding PDFs for a set of data simulated with the same parameters but a different $\theta = -3.049$.

second slope (red dashed line fit) highlights a deviation of the tail from the previous exponential decay, where very intense events are more frequent than expected in the bounded regime.

3.3. Phase dynamics

Let us focus now on the role of the phase dynamics in the formation of these abnormal high-peak events. To this purpose, it is useful to set $E = \rho \exp(i\phi)$ and recast Eqs. (1)-(2) for the field amplitude and phase:

$$\frac{\partial \rho}{\partial z} + \frac{\partial \rho}{\partial t} = T\left[(D-1)\,\rho + y\cos\phi\right] \tag{6}$$

$$\frac{\partial \phi}{\partial z} + \frac{\partial \phi}{\partial t} = -T\left[\theta + \alpha D + \frac{y}{\rho}\sin\phi\right] \tag{7}$$

$$\frac{\partial D}{\partial t} = b\left[\mu - D\left(1+\rho^2\right)\right], \tag{8}$$

where we have neglected the diffusion term to keep the equations simpler (such term is mantained in the simulation). In Eq. (7), we observe that the sign of the right hand side determines the rotation direction of the electric field in the complex plane for fixed z or t. If the first term $\theta + \alpha D$ were null, assuming ρ constant, the equation would be that of a pendulum, with a stable fixed point in 0 and an unstable one in π. Yet the ratio y/ρ in front of the sine is normally very small, because the unstable focus C in the proximity of the origin acts as a repeller that prevents the field amplitude to assume too small values. Therefore the dominant term in Eq. (7) is the first one, which forces the electric field to rotate clockwise or counterclockwise depending on its sign. We can define a critical value of D, $D_c = -\theta/\alpha$ which marks the boundary between the two rotation directions. With our choice of the parameters $D_c \approx 1.013$. If the dynamics of D were fast enough to follow adiabatically that of the field intensity, we could also define a critical amplitude through the stationary equation $D_c = \mu/(1+\rho_c^2)$. With our parameters we have $\rho_c \approx 0.293$. Although the above assumption is not fully confirmed by the simulation, the critical amplitude ρ_c plays a role in the phase dynamics, as will be shown in the following.

In order to compare with the experiment, we computed a histogram in the complex plane $(\mathrm{Re}(E), \mathrm{Im}(E))$ of all the values assumed by the electric field. Fig. 9(a) is the experimental histogram and Fig. 9(b) is the numerical one. A clear similarity between the two histograms is noticeable, especially regarding the presence of an unstable bounded state (yellow area) from

Optics EXPRESS

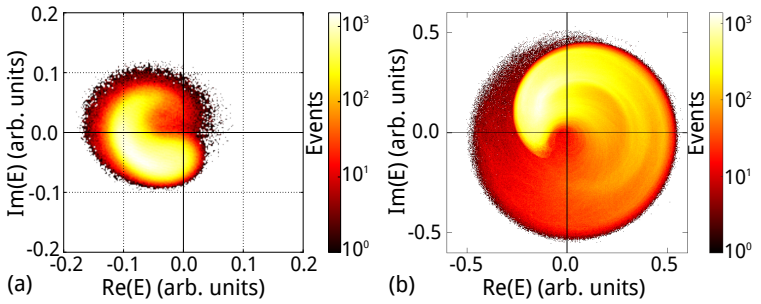

Fig. 9. Histogram of the values assumed by the electric field in the complex plane $(\mathrm{Re}(E), \mathrm{Im}(E))$ in the experimental case (a), computed over 10^4 roundtrips, and in the numerical case (b), computed over 10^5 roundtrips, in order to mantain the same number of events associated to the bounded state.

which rarer events get detached, exploring other areas of the histogram (depicted in red). The reason for the different location of the bounded state between the experimental and numerical picture is due to the fact that the relative phase is measured up to a constant, as explained in section 2.

As illustrated in section 2, from the experiments it was already clear that chirality was playing an important role in the formation of high-peak events: in particular the latter seem to be associated with the appearance of a positive (counterclockwise) chiral charge (see Fig. 4). In the numerical simulations, as we will explain later, we noticed that clockwise phase rotations also play an important role in the formation of abnormal events. Unluckily in the experiment it was impossible to clearly identify the role of clockwise rotations in relation to high-peak events due to the low intensity values of the structures carrying the negative charge, which fell within the experimental noise level. Nevertheless, we can now draw a comparison of the phase dynamics between experimental and numerical data as detailed in the following. Eventually this will allow us to suggest a predictor for the abnormal event, associated with the chirality of the propagating structures. In Fig. 10(a) we plotted the evolution of the phase when approaching an abnormally

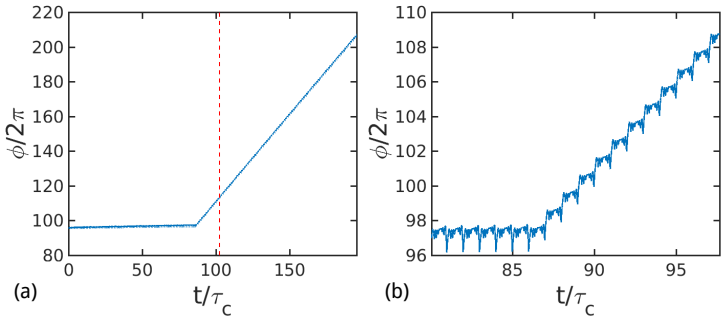

Fig. 10. Evolution of the phase when approaching an abnormally high event: the high-peak event (occurring at the time indicated by the red vertical dashed line) is to be associated with a change in the slope of the phase. In particular in this case we notice an initially balanced situation between the number of positive and negative chiral charges that breaks when the negative chiral charge disappears. A little later an abnormal event takes place.

high event, in a situation similar to the experimental case: here we notice that an initial balance between the number of positive and negative chiral charges is broken by the loss of a negative charge, which gives rise to a change in the slope of the phase. A little later, a high-peak event

Optics EXPRESS

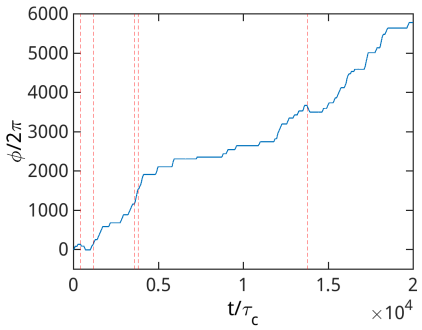

Fig. 11. Total evolution of the phase during 2×10^4 roundtrips. The red vertical dashed lines correspond to five different abnormal events occurring during this time interval.

occurs (highlighted by the red vertical dashed line). In the zoom in Fig. 10(b) it is possible to notice that in the initial plateau for the phase there are both a positive and a negative chiral charge, which then get reduced to a single positive charge. This situation is similar to the one illustrated in section 2 in Fig. 4, where an initially balanced situation with no chiral charges becomes unbalanced through the acquisition of a positive chiral charge, right before the occurrence of an abnormal event. This is not nevertheless the only possible configuration regarding the evolution of the phase before or after the occurrence of abnormal high-peak events. As a common thread we can argue that the occurrence of abnormal events may be associated with a global change in the slope of the phase: however, as it has been observed in the experiment, this change is not to be considered as a precursor since it can occur either before or after the high-peak event itself. To better illustrate this point in Fig. 11 we depicted the total evolution of the phase during a time interval of 2×10^4 roundtrips, the five red vertical dashed lines correspond to five different abnormal events occurring during this time interval. Furthermore from Fig. 11 we can observe that even if sometimes the number of negative chiral charges exceeds the number of positive chiral charges in a single roundtrip (which leads to a negative slope for the phase), the number of positive chiral charges largely exceeds the number of negative ones, as it has already been observed in the experiments: we believe that this strongly asymmetric behavior is to be related to the propagative nature of our system.

It is interesting to analyze also the trajectories in the two phase-space sections $(\mathrm{Re}(E), \mathrm{Im}(E))$ and (D, I) to evidence the phase rotation peculiarities. In Fig. 12 we show the trajectories of the four sections in Fig. 7, where the line color changes from dark green to yellow for increasing time (from the left to the right side of each section). The (unstable) locked states A, B and C of Fig. 5 are highlighted in each figure. The presence of two different time scales in the model has an impact on the intensity excursions, similarly to what occurs in systems lacking propagation in space [20].

In (b) the red vertical dashed line corresponds to the condition $D = D_c = -\theta/\alpha$ relevant for the phase dynamics in Eq. (7), while the red dashed circle in Fig. 12(a) has radius $\rho = \rho_c$ (see the beginning of this Subsection). Although the numerical simulations do not fully support the assumption of adiabatic following for D which led to the definition of ρ_c, it is interesting to note that, as long as the term $(y/\rho)\sin\phi$ is negligible in Eq. (7), when the trajectory enters the circle (where approximately both fixed points A and B lie) it will start rotating clockwise, and as soon as it exits the circle it will again rotate counterclockwise.

In 12(b), we plotted a red (blue) cross every time a full 2π (-2π) counterclockwise (clockwise) phase rotation was reached. The red and blue circles indicate the starting point for the corresponding full rotation. At first we can observe in column 1 of Fig. 12 a mostly bounded

Optics EXPRESS

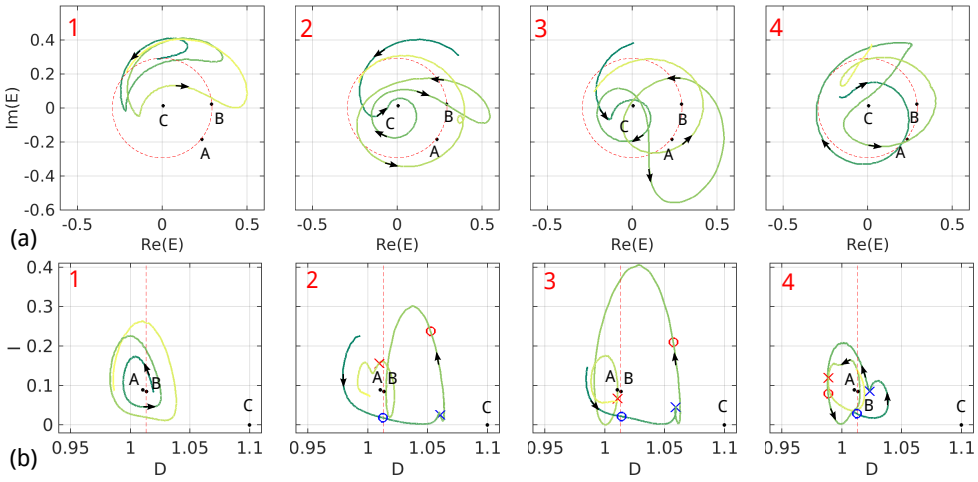

Fig. 12. Phase portrait in the $(\mathrm{Re}(E), \mathrm{Im}(E))$ plane (a) and in the (D, I) plane (b) of the trajectory of the system at fixed roundtrip in the time region close to an abnormal event highlighted in Fig. 7. *A*, *B* and *C* represent the injection locked solutions highlighted in Fig. 5. The red (blue) cross indicates a complete counterclockwise (clockwise) phase rotation, which starts from the point highlighted by the red (blue) circle. As for the dashed red line/circle see text.

regime, where the trajectory of the system remains in a specific area of the complex plane, also highlighted in Fig. 9, without performing any full phase rotations.

Then, in column 2 of Fig. 12, 40 roundtrips before the event, as the trajectory of the system starts to move towards higher values of the population D, we can observe the occurrence of a first clockwise phase rotation (blue circle $\rightarrow$ blue cross) and a second counterclockwise rotation (red circle $\rightarrow$ red cross). We can notice that: i) the clockwise rotation is triggered, for low enough (almost zero) values of the intensity, in the proximity of the condition $D = D_c$; ii) after performing a full -2π rotation (which ends at the blue cross), the system reaches a maximum value of D and then gets repelled to high values of the intensity I due to the repulsive nature of the point C; iii) thanks to a favorable ϕ the term with $\sin\phi$ becomes more and more important in the determination of the sign of the phase equation and, at the point indicated by the red circle in (b), a counterclockwise phase rotation starts forming, which is reinforced when the trajectory approaches the red vertical dashed line, below which the first term of the phase equation becomes positive as well. Such a rotation reaches 2π at the point highlighted by the red cross.

The excursion of the trajectory toward high values of intensity, due to the interplay between these two opposite phase rotations, reaches then its maximum in column 3 of Fig. 12, and, after that, it starts decreasing, as depicted in column 4 of Fig. 12 where the two phase rotations are still present but the trajectory is slowly moving towards lower values of population, eventually evolving into a bounded state as the one in column 1 of Fig. 12, where phase rotations will disappear (usually not at the same time).

We observed that this mechanism is common to all the high-peak events in the tail of the distribution in Fig. 8(a) and could serve as a predictor of abnormal events. In Fig. 13 we consider a zoom of the spatio-temporal diagram for the intensity I of the electric field (a) and for the population D (b) centered on an abnormal event (highlighted by the green circle). Here we depicted with a light blue (orange) line the clockwise (counterclockwise) phase rotations.

The mechanism illustrated in Fig. 12 is here visible: at first a negative chiral charge (light blue) appears; then, around 100 roundtrips before the event, a positive chiral charge (orange)

Optics EXPRESS

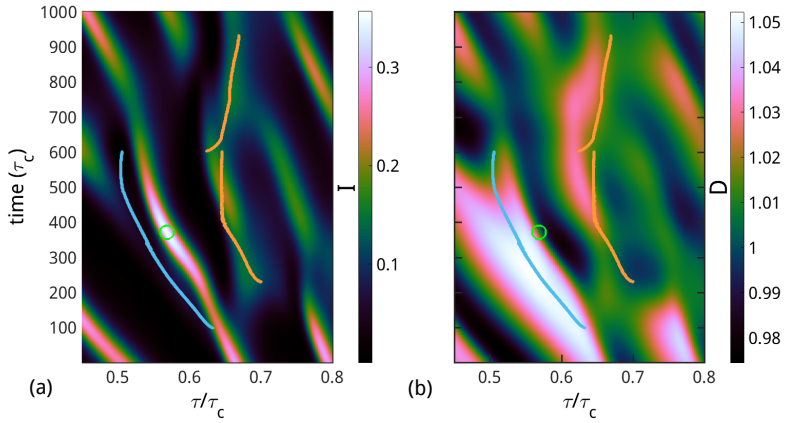

Fig. 13. Spatio-temporal diagram of the intensity I of the electric field (a) and of the carrier population D (b). The light blue (orange) line corresponds to clockwise (counterclockwise) phase rotations, the abnormal event has been highlighted by the green circle.

is formed, but the simultaneous presence of a clockwise phase rotation is necessary to observe the abnormally high event; finally, both charges disappear, at different times. We would like to emphasize that clockwise rotations always occur only for high values of population, when the intensity of the electric field approaches zero (as in Figs. 12(b) and 13(b)), and it is the interplay of clockwise and counterclockwise phase rotations that gives rise to the observed abnormal events. In fact, it may happen that clockwise rotations occur without any positive chiral charge in their proximity: such a configuration does not give rise to high-peak events.

We observe that phase rotations may be associated with a transient exploration of the PS regime, unstable for this choice of parameters: in particular, in a stable PS regime, counterclockwise rotations would correspond to stable PSs. However clockwise rotations cannot be associated with unstable PSs [25], due to the asymmetric nature of this propagative system.

4. Conclusions

We have studied both experimentally and numerically the occurrence of abnormal events in a highly multimode semiconductor laser with coherent optical injection, in a configuration close to the roll pattern regime. The experimental and numerical data present an excellent agreement, corroborated by a detailed statistical analysis. In the regime under study, where the roll pattern is modulationally unstable, both the distribution of the field intensity and the peak amplitude are bounded but present a characteristic size separating two types of events. This scale separation emerges as different exponential decays in the distribution of the intensity and as a strong deviation from Gaussianity in the peak amplitude distribution. In this parametric regime phase solitons are unstable but we observed that the phase dynamics of the system plays a crucial role in the formation of the events pertaining to the distribution tail. In particular, the interplay between $\pm 2\pi$ phase rotations appears to be related to the observation of abnormally high events and it is absent in other parametric regions, not exhibiting big excursions in intensity. The observed phase and amplitude dynamics is strongly reminiscent of the regime of defect mediated turbulence [37] or vortex turbulence that has been recently associated with optical rogue waves in an oscillatory two-dimensional transverse spatial system with cohrent forcing [24]. However a full experimental and numerical characterization of the emergence of phase defects and their statistics in the context of this non-instantaneous and propagative oscillatory medium remains to be performed.